# Reduced sulfatide content in deferoxamine-induced senescent HepG2 cells

Silvia Ghislanzoni [a,*], Gaia Martina Sarcinelli [a], Arianna Bresci [b], Francesco Manetti [b], Dario Polli [b,d], Antonella Tomassetti [c], Maria Teresa Radice [c], Italia Bongarzone [a]

[a] *Department of Advanced Diagnostic, Fondazione IRCCS Istituto Nazionale dei Tumori, Via G. Amadeo 42, Milan 20133, Italy*
[b] *Department of Physics, Politecnico di Milano, Piazza L. da Vinci 32, 20133 Milan, Italy*
[c] *Department of Experimental Oncology, Fondazione IRCCS Istituto Nazionale dei Tumori, Via G. Amadeo 42, Milan 20133, Italy*
[d] *CNR Institute for Photonics and Nanotechnologies (IFN), Piazza L. da Vinci 32, 20133 Milan, Italy*

## ARTICLE INFO

## ABSTRACT

Iron chelators, such as deferoxamine, exert an anticancer effect by altering the activity of biomolecules critical for regulation of the cell cycle, cell metabolism, and apoptotic processes. Thus, iron chelators are sometimes used in combination with radio- and/or chemotherapy in the treatment of cancer. The possibility that deferoxamine could induce a program of senescence similar to radio- and/or chemotherapy, fostering adaptation in the treatment of cancer cells, is not fully understood. Using established biochemical techniques, biomarkers linked to lipid composition, and coherent anti-Stokes Raman scattering microscopy, we demonstrated that hepatocellular carcinoma-derived HepG2 cells survive after deferoxamine treatment, acquiring phenotypic traits and representative hallmarks of senescent cells. The results support the view that deferoxamine acts in HepG2 cells to produce oxidative stress-induced senescence by triggering sequential mitochondrial and lysosomal dysfunction accompanied by autophagy blockade. We also focused on the lipidome of senescent cells after deferoxamine treatment. Using mass spectrometry, we found that the deferoxamine-induced senescent cells presented marked remodeling of the phosphoinositol, sulfatide, and cardiolipin profiles, which all play a central role in cell signaling cascades, intracellular membrane trafficking, and mitochondria functions. Detection of alterations in glycosphingolipid sulfate species suggested modifications in ceramide generation, and turnover is frequently described in cancer cell survival and resistance to chemotherapy. Blockade of ceramide generation may explain autophagic default, resistance to apoptosis, and the onset of senescence.

## 1. Introduction

Iron is an essential element used by living cells for many cellular processes (Hentze et al., 2004). However, iron has been linked to various diseases, including cancer. Iron bioavailability is rate-limiting during DNA synthesis; therefore, cancer cells require more iron as they undergo rapid division. Cancer tissues, across virtually all solid cancer types, have been widely observed to present with (local) iron accumulation (Torti and Torti, 2013). Despite being non-replicative, senescent cells, whether induced by irradiation, chemotherapy, or oncogenes, also accumulate vast amounts of intracellular iron, affecting the levels of proteins involved in iron homeostasis. One possible explanation for iron overload in senescent cells concerns dysfunctional lysosomes, a well-known feature of senescence that leads to impaired ferritin degradation with consequent iron accumulation (Masaldan et al., 2018).

Excessive iron is toxic due to its ability to generate reactive oxygen species (ROS) and can even trigger cell death. Ferroptosis is a type of oxidative cell death induced by of iron-mediated lipid peroxidation (Stockwell et al., 2017; Xie et al., 2016). However, senescent cells exhibit alterations in iron acquisition and storage, with impeded iron-mediated cell death pathways (Masaldan et al., 2018).

The use of iron chelators, such as deferoxamine (DFO), deferiprone, and deferasirox, which are conventionally administered for the treatment of iron-loaded diseases (Chaston and Richardson, 2003), is a developing strategy for senescence-related disorders with the aim of sequestering iron from usage (Nakamura et al., 2019; Ward et al., 2014). As tumor cells are strongly dependent on iron for their growth and proliferation, iron chelators also work against cancer as therapeutic agents (Heath et al., 2013). Several clinical studies have shown that DFO exhibits antitumor activity in patients with neuroblastoma, leukemia, or hepatocellular carcinoma (Donfrancesco et al., 1990; Estrov et al., 1987; Yamasaki et al., 2011).

Mechanistically, DFO triggers the degradation of ferritin within lysosomes and binds the released iron, causing its retention in the lysosomal compartment and impeding its release into the cytoplasm (Yambire et al., 2019). This leads to a hypoxia-like response, loss of mitochondrial function, inhibition of the activities of several essential enzymes that require iron, changes in mitochondria metabolism, and lipid droplet (LD) accumulation. The localization of LDs at the borders of the mitochondria network suggests impaired mitophagy (Al Tameemi et al., 2019; De Bortoli et al., 2018).

This vicious feedback loop between lysosomes and mitochondria plays a functional role in cellular senescence, including that induced by anticancer therapy, in which structural alterations and the malfunction of both lysosomes and mitochondria account for the majority of senescent changes.

Therapy-induced cellular senescence is relevant to clinical practice because it can contribute to tumor progression and resistance to therapy. However, detection and characterization of senescent cancer cells are still challenging (Prasanna et al., 2021). Recent research has documented that senescent cells exhibit global alterations in lipid composition, but the mechanisms underlying their role in the development of senescence are yet to be clarified and the lipidomics of senescent cells are yet to be thoroughly explored (Hamsanathan and Gurkar, 2022; Pils et al., 2021).

In this study, we aimed for a deeper characterization of the metabolic changes related to therapy-induced senescence and the discovery of novel biomarkers for senescent cancer cells. We adopted DFO treatments to induce mitochondrial damage and oxidative stress in rapidly growing HepG2 hepatocellular carcinoma cells. In addition to a predominantly cytotoxic response, we observed a typical senescence response, with loss of proliferative capacity. Our study also highlights senescence-associated modifications in the profiles of phosphoinositols (PIs), sulfatides, and cardiolipins (CLs).

## 2. Materials and methods

### 2.1. Chemicals and solvents

All solvents (ULC grade) were purchased from Merck (Italy) unless stated otherwise. 9-Aminoacridine (9AA) was purchased from Sigma-Aldrich (Italy). ITO glass slides were obtained from Bruker Daltonics GmbH (Bremen, Germany). Chloroform and ethanol (HPLC grade) were purchased from Sigma-Aldrich (Italy). Methanol (LC-MS grade) was from Fisher Scientific (Italy).

### 2.2. Cell culture

HepG2 cells were purchased from American Type Culture Collection (ATCC, Manassas, VA, USA; ATCC number: HB-8065) and maintained in Dulbecco's modified Eagle medium (DMEM; Gibco, Italy) supplemented with 10% fetal bovine serum (FBS; Gibco) at 37 °C and 5% $CO_2$.

### 2.3. Treatments

DFO (Merk) was diluted in distilled water at a final concentration in culture medium of 100 μM. Cells were seeded at a density of 300,000 cells/mL, exposed to DFO 24 h after plating, and cultured in its presence for 72 h or 7 days.

### 2.4. β-Galactosidase staining

Following the instructions of the SA-β-gal Staining Kit (Cell Signaling, Massachusetts, USA), control cells and 72 h and 7-day DFO-treated cells were washed with PBS and then fixed with fixation solution (provided by the kit) for 15 min at 25 °C. After rinsing with PBS twice, cells were stained with the β-Gal staining solution and incubated at 37 °C overnight in a dry incubator, and then observed under a light microscope (Leica DM IRB microscope, Leica Microsystems, Wetzlar, Germany).

For quantification of β-galactosidase activity, control and 7-day DFO-treated cells were stained with Green BioTracker 519 B-Gal Dye (Invitrogen, USA). Cells were incubated with 1 μM Green BioTracker 519 B-Gal Dye and incubated for 15 min at 37 °C, rinsed, and imaged using an epifluorescence microscope (Eclipse T*i*2-e, Nikon). The fluorescence intensity derived from the marker was measured using FiJi (ImageJ).

### 2.5. Oil Red O

For Oil Red O staining, the cells were washed with PBS (Lonza, Italy) and then fixed with 4% formaldehyde for 10 min at room temperature. A stock solution of Oil Red O (0.5%) was diluted to 60% in isopropyl alcohol with water (3:2, V/V) and used to stain cells for 20 min in the dark, and then washed carefully with water three times. After death, cells were observed under a light microscope (Leica DM IRB microscope, Leica Microsystems).

### 2.6. ATP measurement

Following the instructions of the ATP Colorimetric/Fluorometric Assay Kit (Sigma-Aldrich, Missouri, USA), control cells and 72 h and 7-day DFO-treated HepG2 cells were lysed with ATP Assay Buffer (100 μL/$10^6$ cells) and deproteinized using 10 kDa MWCO spin filters. A 15 μL aliquot of each sample and 2 μL of ATP Converter were added into duplicate wells of a 96-well plate and brought to a final volume of 50 μL with ATP Assay Buffer. For each sample, a blank was prepared by omitting the ATP Converter. Five standards were prepared for fluorometric detection as indicated in the kit protocol. The fluorescence emitted from the samples and standards was measured using SPARK Tecan (SW SPARKCTL. Magellan V2.2 STD 2PC, GmbH, Austria).

### 2.7. Confocal microscopy

Mitochondria and lysosomes were stained in live cells using Mito-Tracker Deep Red FM and LysoTracker Deep Red FM (Invitrogen), respectively, diluted to a final concentration of 100 nM in the culture medium as suggested by the producer. Briefly, cells were incubated with the probe at 37 °C and 5% $CO_2$ for 45 min, gently washed with PBS, fixed with 4% paraformaldehyde (PFA, Sigma-Aldrich) for 10 min, and permeabilized with 1% BSA + 0.2% Triton X/PBS for 30 min. Subsequently, the cells were blocked with 10% normal goat serum (Cell Signaling) for 1 h and incubated overnight at 4 °C. The following primary antibodies were used: phospho-histone H2A.X (Ser139) (20E3) rabbit mAb (Cell Signaling) diluted 1:1000 and LC3B rabbit mAb (Cell Signaling) diluted 1:500. The cells were then washed with Triton X 0.2%/PBS and incubated for 1 h at room temperature with the secondary antibody, goat anti-rabbit IgG (H+L) highly cross-adsorbed secondary antibody Alexa Fluor 546 (Invitrogen), diluted 1:500. Samples were mounted with DAPI-containing anti-fade reagent (ProLong Gold, Life Technologies, USA). Confocal microscopy was performed using a Leica TCS SP8 X confocal laser scanning microscope (Leica Microsystems GmbH).

### 2.8. Flow cytometry

Cell cycle analysis was performed on control cells and 72 h and 7-day DFO-treated cells and monitored using a BD FACSCanto instrument (BD Biosciences San Jose, CA, USA). Upon treatment, trypsinized cells were fixed with 70% EtOH and incubated overnight with 50 μg/mL propidium bromide (Cell Signaling) in the presence of 10 μg/mL RNase DNase free (Thermo Fisher). Data analysis was performed using ModFit LT™ (Verity Software House).

### 2.9. Western blot

Cells were washed with cold PBS, scraped, and lysed with 5% SDS/ 125 mM Tris-HCl (pH 6.8) at 99 °C. Protein levels were assessed by Western blotting. Protein concentrations in the samples were determined using the BCA™ protein assay kit (Pierce). Proteins were separated by 12% SDS-PAGE, and then transferred to polyvinylidene difluoride (PVDF) membranes. Membranes were blocked and incubated overnight at 4 °C with the following primary antibodies: ferritin (Abcam, 1:1000), transferrin receptor (Abcam, Cambridge, UK, 1:1000), LC3B (Cell Signaling, 1:1000), PARP (Cell Signaling, 1:1000), PI3K (Cell Signaling, 1:1000), Akt (Cell Signaling, 1:1000), phospho-Akt (Cell Signaling, 1:1000), phospho-H2A.X (Ser139) (Cell Signaling, 1:000), and survivin (Cell Signaling, 1:1000). Membranes were washed and incubated with anti-rabbit and anti-mouse ECL antibodies (GE Healthcare) for 1 h at room temperature and washed again. After antibody incubation, band intensity was detected via chemiluminescence and imaged using an Azure Biosystems c600.

### 2.10. Forward coherent anti-stokes Raman scattering (CARS)

Cells were cultured on 22x22x 0.17 mm quartz slides. At the desired endpoint, untreated (control) and DFO-treated cells were gently washed with PBS (Lonza) and fixed with 4% PFA for 10 min. Each quartz slide was mounted upside-down in the middle of a clean 25x50x 0.17 mm quartz slide with the cells placed in-between. The four edges of each smaller slide were carefully sealed to the bigger one using nail polish. We built a multimodal microscope with off-the-shelf components featuring seven different NLO modalities, including CARS (Lu et al., 2015). The laser source delivers 780 nm pump pulses and 950–1050 nm tunable Stokes pulses with 1 picosecond duration, matching the CH-stretching region of the Raman vibrational spectrum (2800–3100 cm$^{-1}$). CARS imaging was performed at 2850 cm$^{-1}$, corresponding to the CH$_2$-stretching vibrational mode of lipids. The percentage of LD area per cell area was calculated by thresholding raw 2850 cm$^{-1}$ CARS images, and then normalizing the area above the threshold over the total cell area outlined from co-registered light transmission images. The threshold was the same for all control and DFO cells and chosen to distinguish lipid accumulations from the cytosol signal. LD concentrations were measured as the square root of thresholded 2850 cm$^{-1}$ CARS images, as the CARS signal scales quadratically with the concentration of scatterer in the focal volume (Lu et al., 2015).

### 2.11. Mass spectrometry

#### 2.11.1. Lipid solubilization

Control and DFO-treated HepG2 cells were pelleted and washed with PBS (Lonza) three times. The extraction of lipids from the obtained pellets was performed using Bligh and Dyer's method (Breil et al., 2017). Briefly, lipids were extracted from the pellet by adding 300 μL of chloroform/methanol (2:1, v/v). The suspension was then mixed for 15 min at 1400 rpm and sonicated for 4 min. Deionized water (100 μL) was added to separate the organic phase from the aqueous phase, and the suspension was mixed for 1 min before centrifuging at 3000 g for 5 min at 20 °C. The organic phase (lower layer) containing lipids was collected in a clean tube and dried in a SpeedVac centrifuge. Lipids were then resuspended in an appropriate volume of 2-propanol/ACN (60/40, v/v) and sonicated for 4 min. At this point, 1 μL of lipid suspension was mixed with 2 μL of 9-AA matrix in a new vial. Next, 1 μL of the mix was layered on the MALDI target plate and left to dry.

#### 2.11.2. MS analysis

Lipids were analyzed in negative-ion mode using a Bruker UltrafleXtreme MALDI TOF MS operating in reflectron mode and equipped with a frequency-tripled 355 nm Nd:YAG laser at repetition rates up to 10 kHz. Data acquisition was controlled by flexControl 3.4 software

(Bruker Daltonics). The mass spectra were acquired over the mass-to-charge ratio ($m/z$) range of 800–1600 in ion Reflectron TOF mode. The laser power was adjusted to a point just above the ionization threshold of the sample with 1000 laser shots per acquisition. Five acquisitions were averaged for each individual spectrum. Tandem mass spectrometry (MS/MS) analysis was performed using a laser ionization fragmentation technology (LIFT) approach as described by Suckau et al. (2003). Characteristic product ions of precursor ions in the MS/MS spectrum were used to identify the lipid class by searching accurate MS/MS fragmentation pattern data in LIPID MAPS (Lipidomics Gateway, http://www.lipidmaps.org/). To compensate for the relatively low resolving power of approximately 5000 at $m/z$ 885.56, tentative assignments were made only if the proposed lipid species were previously described in the literature. Raw data pre-processing was performed using SimLipid Software (http://www.premierbiosoft.com). CSV files were directly imported into MetaboAnalyst 5.0 software (www.MetaboAnalyst.ca/faces/home.xhtml) for downstream univariate statistical analysis (volcano plot) and multivariate statistical analyses, such as partial least squares discriminant analysis (PLS-DA) and hierarchical clustering (heatmap). The variables were log2-transformed, and Pareto scaling with mean centering was applied for normalization (Wolrab et al., 2022). To visualize the whole data set of changes within and across different DFO treatments and control samples, we used the self-organizing maps (SOM) algorithm in MetaboAnalyst.

#### 2.11.3. Preparation of samples for MALDI imaging analysis

HepG2 cells were seeded in silicone two-well chambers mounted on indium-thin-oxide (ITO) slides at a density of 12,500 cells/well. DFO treatments were carried out on the slides. At the end of the treatment, the culture medium was removed and cells washed three times with PBS. ITO slides were then stored in a vacuum desiccator until matrix deposition. Optical images were acquired prior to matrix application. A TM-sprayer nebulizer (HTX Technologies) was used to apply the matrix for MALDI-MSI analysis. The 9-AA matrix (Sigma-Aldrich) was prepared in 2-propanol/ACN (60/40, v/v) to a final concentration of 10 mg/mL. For its application, the temperature of the nozzle was set to 80 °C, the pressure 10 psi, and the LC pump flow rate 0.12 mL/min. After matrix application, samples were left in the desiccator until MALDI-MSI spectra acquisition. Samples were analyzed in negative-ion mode using a Bruker UltrafleXtreme MALDI TOF mass spectrometer operating in reflectron mode and equipped with a frequency-tripled 355 nm Nd:YAG laser at repetition rates up to 10 kHz. Laser power and laser focus position were manually fine-tuned before each acquisition to ensure optimal data quality and comparable signal intensity. Imaging experiments were controlled by FlexImaging 4.1 software (Bruker Daltonics, Billerica, MA, USA) with a raster size of 50 μm. At each raster position, 200 laser shots were summed to generate a representative spectrum for each pixel with the digitizer sampling rate at 1.25 GS/s. Spectra were acquired in the $m/z$ 800–1600 range at each pixel position. The data from the analysis of untreated or DFO-treated samples were co-registered to the acquired MALDI-MSI data and normalized to total ion count (TIC) and visualized by FlexImaging. SCiLS lab version 2022 Pro (SCiLS GmbH, Bremen, Germany) was used for data analysis. Briefly, MALDI-MSI reduced datasets were imported into SCiLS Lab (Thiele et al., 2014), converted to the SCiLS SL format, and then normalized to the TIC. SCiLS was used to obtain the spatial distribution and create box and dot plots of normalized signal peak intensities, which showed significant differences between control and 72 h DFO-treated samples.

#### 2.11.4. Tandem mass spectrometry

Tandem mass spectrometric analysis was performed on molecular species of interest (some major abundant lipid classes) using LIFT mode as described above.
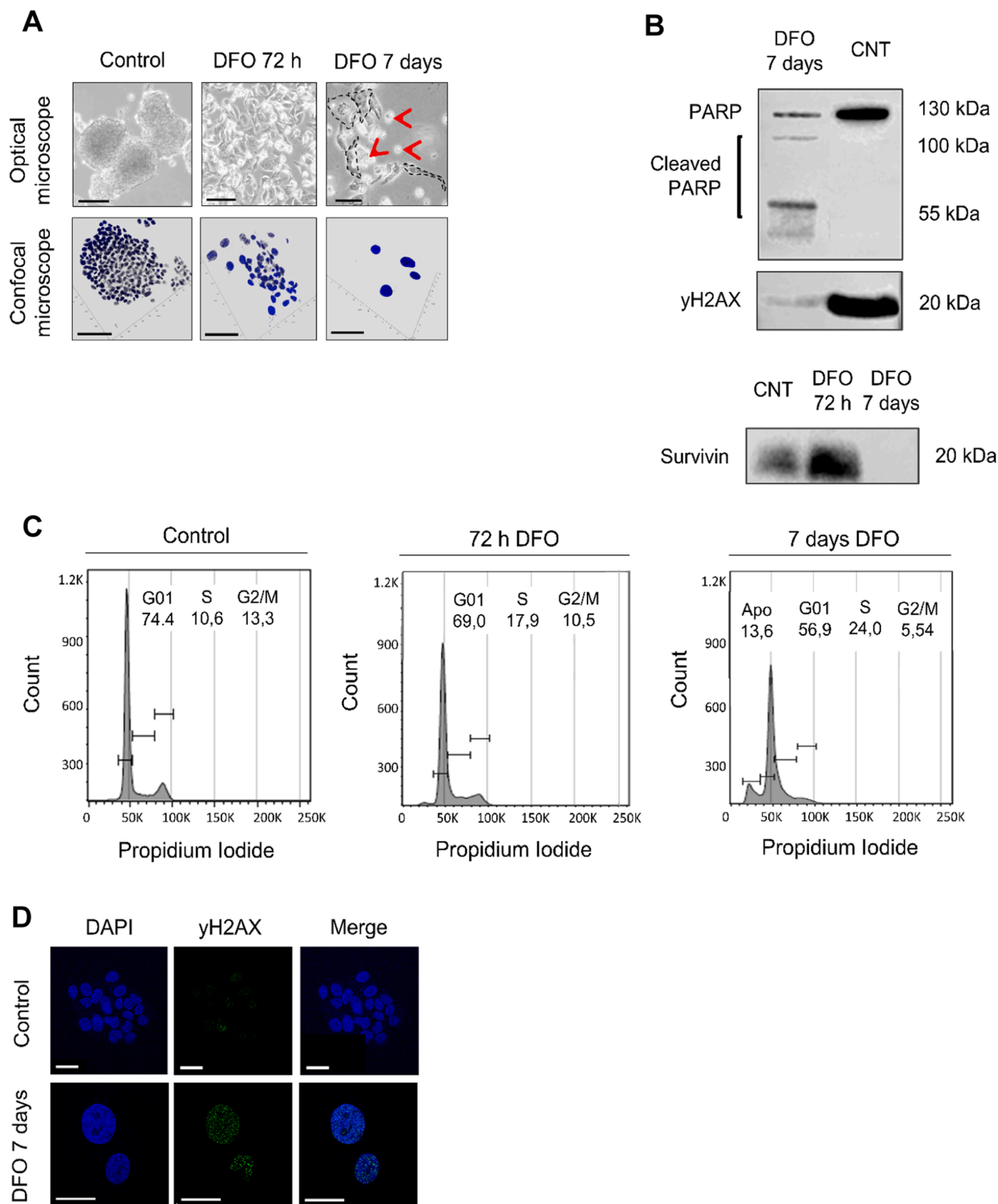
**Fig. 1.** DFO treatment of HepG2 cells induces either apoptosis or extensive morphological modifications, with the surviving cells losing their 3D structure and undergoing cell cycle arrest and DNA damage. **(A)** Representative pictures of HepG2 cells before and after DFO treatment acquired with an optical microscope (scale bar = 100 μm) and a confocal microscope after staining with DAPI (3D visualization; scale bar = 50 μm). Enlarged cells after 7 days of DFO treatment are delineated with a discontinuous black line; red arrows indicate apoptotic cells. **(B)** Protein expression levels of PARP, yH2AX, and survivin in untreated and treated HepG2 cells determined by immunoblotting. Graphs representing the immunoblots bands quantification are shown in Supplementary File 2, Figs. S3, S4, S7, S8. **(C)** Cell cycle analysis of untreated, 72 h DFO-treated, and 7-day DFO-treated HepG2 cells. **(D)** Representative images of control and 7-day DFO-treated HepG2 cells stained for phospho-H2AX foci (green) and DAPI (blue). Cells were observed and imaged using a confocal microscope. Scale bar = 25 μm.

## 3. Results

### 3.1. DFO treatment leads to cell flattening and DNA damage

As observed by both optical and confocal microscopy after staining nuclei with DAPI, HepG2 cells spontaneously formed spheroid-like and connected three-dimensional (3D) structures, even after trypsinization and re-seeding as single-cell suspension. However, treatment with 100 μM DFO for 72 h was sufficient to cause the cells to shift toward a mainly two-dimensional (2D) growth pattern with loss of their spheroid shape (Fig. 1A). Prolonged DFO treatment (7 days) induced apoptosis of most cells, as shown by cleavage of the protein PARP (Fig. 1B). PARP plays a role in various cellular processes, including DNA repair and apoptosis (Morales et al., 2016). Accordingly, cell cycle analysis of control and DFO-treated HepG2 cells showed impairment of all cell cycle phases after 72 h of treatment with the slight presence of a sub-G0 peak reminiscent of apoptotic cells (Fig. 1C). After 7 days of treatment, the G2

phase disappeared and approximately 14% of cells were in sub-G0 phase. However, a small percentage of cells survived and the 2D growth pattern induced by DFO was maintained, with the surviving cells at 7 days appearing enlarged and flattened (Fig. 1A).

Given the extensive morphological modifications of the treated cells and cell cycle alterations observed after DFO treatment, we asked whether DFO caused detectable DNA damage by analyzing the H2AX phosphorylation level, a molecular marker of DNA double-strand breaks (hereafter, γH2AX foci) (Mah et al., 2010), using immunofluorescence and immunoblotting. Phosphorylation of H2AX at Ser 139 (γ-H2AX) occurs quickly after DNA damage, is abundant, and correlates well with each DNA double-strand break; therefore, it is a sensitive biomarker for DNA damage (Sharma et al., 2012). As we observed a dramatic increase in γH2AX foci after 7 days of DFO treatment compared to control samples according to immunofluorescence (Fig. 1D) and immunoblotting (Fig. 1A), we concluded that cells underwent DNA damage upon DFO treatment.
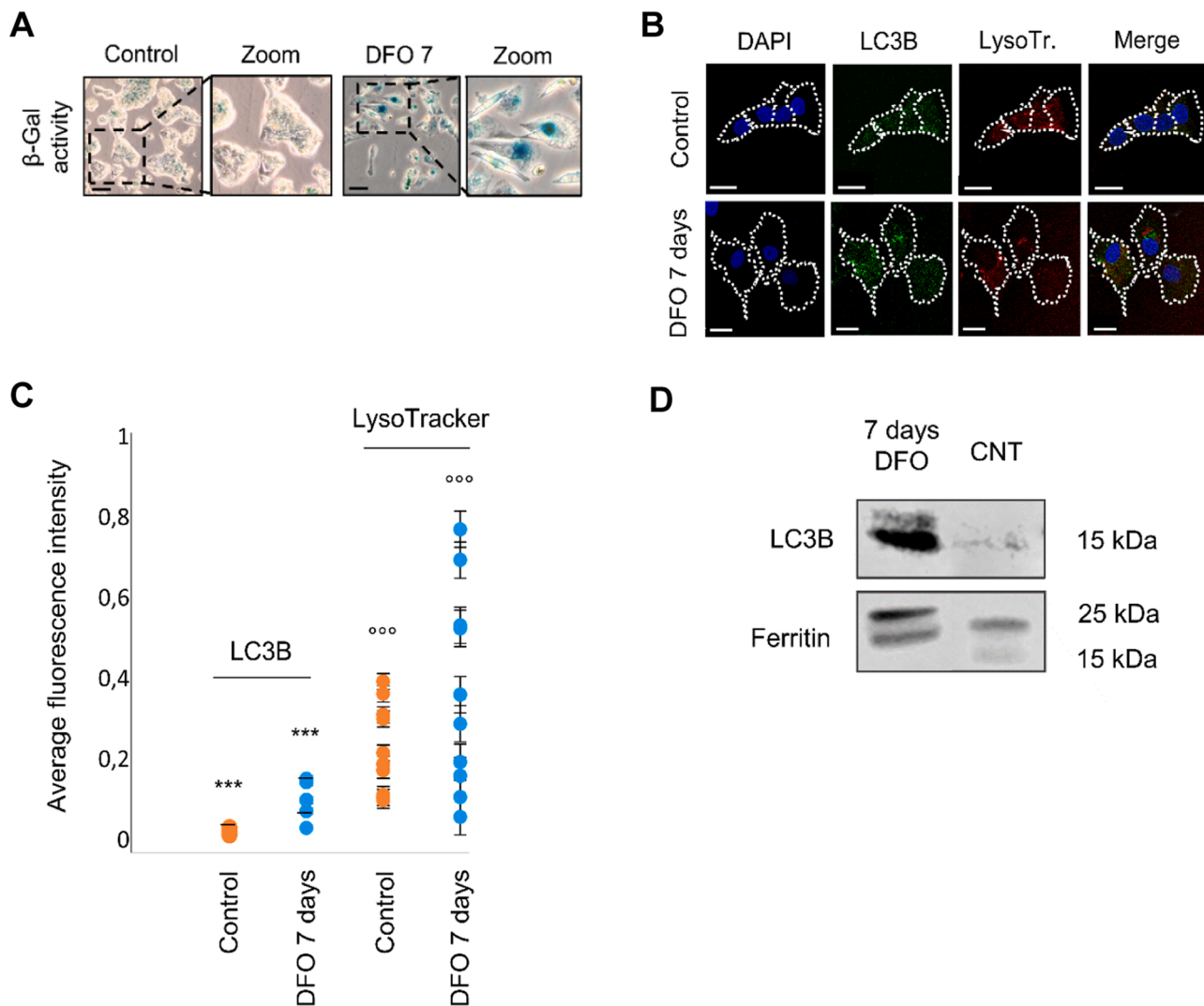


**Fig. 2.** DFO treatment triggers the development of cellular senescence with alteration of the lysosomal compartment. **(A)** Representative images of untreated and 7-day DFO-treated HepG2 cells stained for β-galactosidase activity with X-Gal (blue). Cells were observed and imaged using an optical microscope. Scale bar = 100 μm. **(B)** Representative images of control and 7-day DFO-treated HepG2 cells stained for lysosomes (red), LC3B (green), and DAPI (blue). Cells were observed and imaged using a confocal microscope. Scale bar = 25 μm. **(C)** Dot plot showing the changes in the average fluorescence intensities derived from Alexa Fluor 546-bound anti-LC3B and LysoTracker Deep Red in control vs. DFO-treated HepG2 cells. The cells were visualized with a confocal microscope, and the 3D images of 20 cells for each condition were randomly chosen and analyzed using ImageJ software. The fluorescence intensities relative to lysosomes and LC3B were both significantly increased after treatment with DFO. * **p<0.001, °°°p<0.001 (comparing 7-day DFO-treated HepG2 cells to their corresponding controls). **(D)** Protein expression levels of LC3B and ferritin in untreated HepG2 cells and HepG2 cells after 7 days of DFO treatment according to immunoblotting. Graphs representing the immunoblots bands quantification are shown in Supplementary File 2, Figs. S5, S6, S8.

Notably, survivin was depleted after 7 days of DFO treatment, when cells exhibited evident senescence-associated morphology (Fig. 1A). This is consistent with cancer cells having high levels of the protein but senescent cancer cells often being survivin-depleted; this is particularly true for senescent cells expressing p53 with inhibited PARP activity and impaired DNA damage repair (Véquaud et al., 2016), all properties of our cellular model.

Notably, the changes after DFO treatment, such as cell cycle impairment and apoptosis with a small percentage of cells surviving; the surviving cells acquiring an enlarged, flattened phenotype; the accumulation of γH2AX foci (a sensor of DNA damage); and depletion of survivin are all common features of therapy-induced senescence in cancer cells (Gorgoulis et al., 2019; Prasanna et al., 2021).

### 3.2. DFO treatment triggers the development of cellular senescence

To verify that DFO treatment triggers cellular senescence in HepG2 cells, control and 7-day DFO-treated cells were stained for β-galactosidase activity with X-gal (Fig. 2A), a widely accepted molecular marker of senescence (Lee et al., 2006). We observed a markedly increased positivity to the staining after DFO treatment. Weak positivity to the staining was also observed in the control samples within the spheroid-like structures, attributed to the presence of senescent cells in the inner layers of the spheroids, which is a known characteristic of 3D cell aggregates (Gilazieva et al., 2020). We quantified β-galactosidase activity by staining with the fluorescence marker BioTracker 519 B-Gal Green Dye; cells were imaged and the fluorescence intensity derived from the marker measured using ImageJ. A statistical comparison between control and 7-day DFO-treated cells (50 cells chosen randomly for each condition) showed a significantly higher average fluorescence intensity in DFO-treated cells ($p < 0.001$, data not shown). Representative images are found in Supplementary File 2 (Fig. S11).

Because lysosomes are the cellular components that undergo the most marked changes when senescence develops (Park et al., 2018), we investigated the lysosomal network of untreated and 7-day DFO-treated HepG2 cells. Fluorescent staining of lysosomes and autophagy-related protein LC3B showed a visible increase in the fluorescence intensity for lysosomes and an even more dramatic increase for LC3B staining after DFO treatment (Fig. 2B). To confirm these results, we measured the average fluorescence intensities corresponding to the lysosomal and LC3B compartments. The fluorescence intensities relative to lysosomes and LC3B were both significantly increased after 7 days of DFO treatment ($p<0.001$; Fig. 2 C). The increased number of LC3B puncta after DFO treatment was further confirmed by immunoblotting (Fig. 2D). These results align with the notion that senescent cells have an extended lysosomal compartment (Park et al., 2018).

Taken together, these data indicate that the cells that survived DFO treatment were senescent.

### 3.3. DFO treatment induces senescence by causing mitochondrial alterations

Degradation of the ferritin protein after DFO treatment in our model was confirmed by immunoblotting; ferritin levels were markedly decreased after 72 h or 7 days of DFO treatment compared to control (Fig. 2B).

Mitochondria are major hubs of iron accumulation and use (Garciaz et al., 2022), and DFO sequesters iron within the lysosomes, making it unavailable for mitochondria (Moiseeva et al., 2009; Wang et al., 2003). Therefore, we investigated whether the occurrence of senescence after DFO treatment in HepG2 cells is linked to an alteration in mitochondrial morphology and functionality. We stained control and DFO-treated HepG2 cells with MitoTracker and performed a confocal analysis. Treatment with DFO markedly affected the mitochondrial morphology,
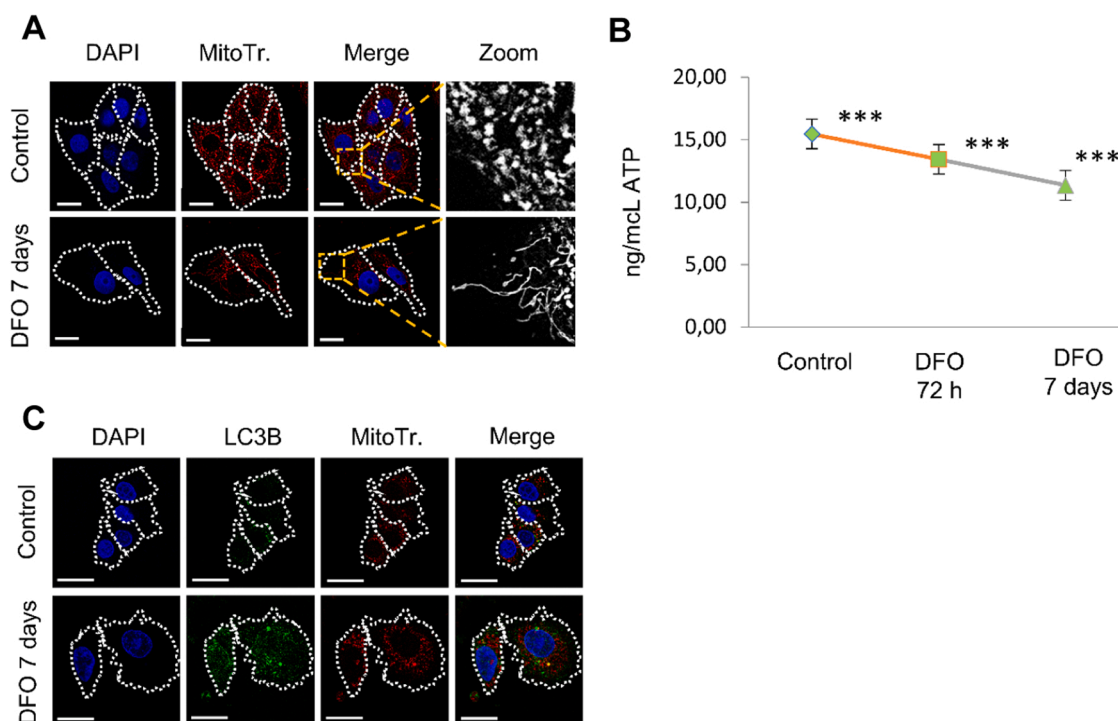
**Fig. 3.** DFO leads to altered morphology and function of the mitochondria network. **(A)** Representative images of control and 7-day DFO-treated HepG2 cells stained for mitochondria (red) and DAPI (blue). In gray are the details of the mitochondria network for each condition. Borders of the cells are delineated with a discontinuous white line. Cells were observed and imaged using a confocal microscope. Scale bar = 25 μm. **(B)** Amount of ATP produced by control cells and 72 h and 7-day DFO-treated HepG2 cells. *** $p < 0.001$ (comparing the control group and the two treated groups and between the two treated groups). **(C)** Representative images of control and 7-day DFO-treated HepG2 cells stained for mitochondria (red), LC3B (green), and DAPI (blue). Cells were observed and imaged using a confocal microscope. Scale bar = 25 μm.

as mitochondria visibly lost their round, compact shape and became elongated, thin, and filamentous (Fig. 3 A).

To verify the impact of DFO-induced iron starvation on the functionality of mitochondria, we measured ATP production in control cells and 72 h and 7-day DFO-treated HepG2 cells. We observed a significant decrease in the concentration of ATP derived from the 72 h DFO-treated samples compared to control (p<0.001) and an even more dramatic decrease after 7 days of DFO treatment (p<0.001; Fig. 3B). Taken together, the data show that DFO, by sequestering iron into lysosomes, causes alterations in the morphology and functionality of mitochondria, likely due to mitochondrial iron depletion, with impaired mitochondrial ATP production.
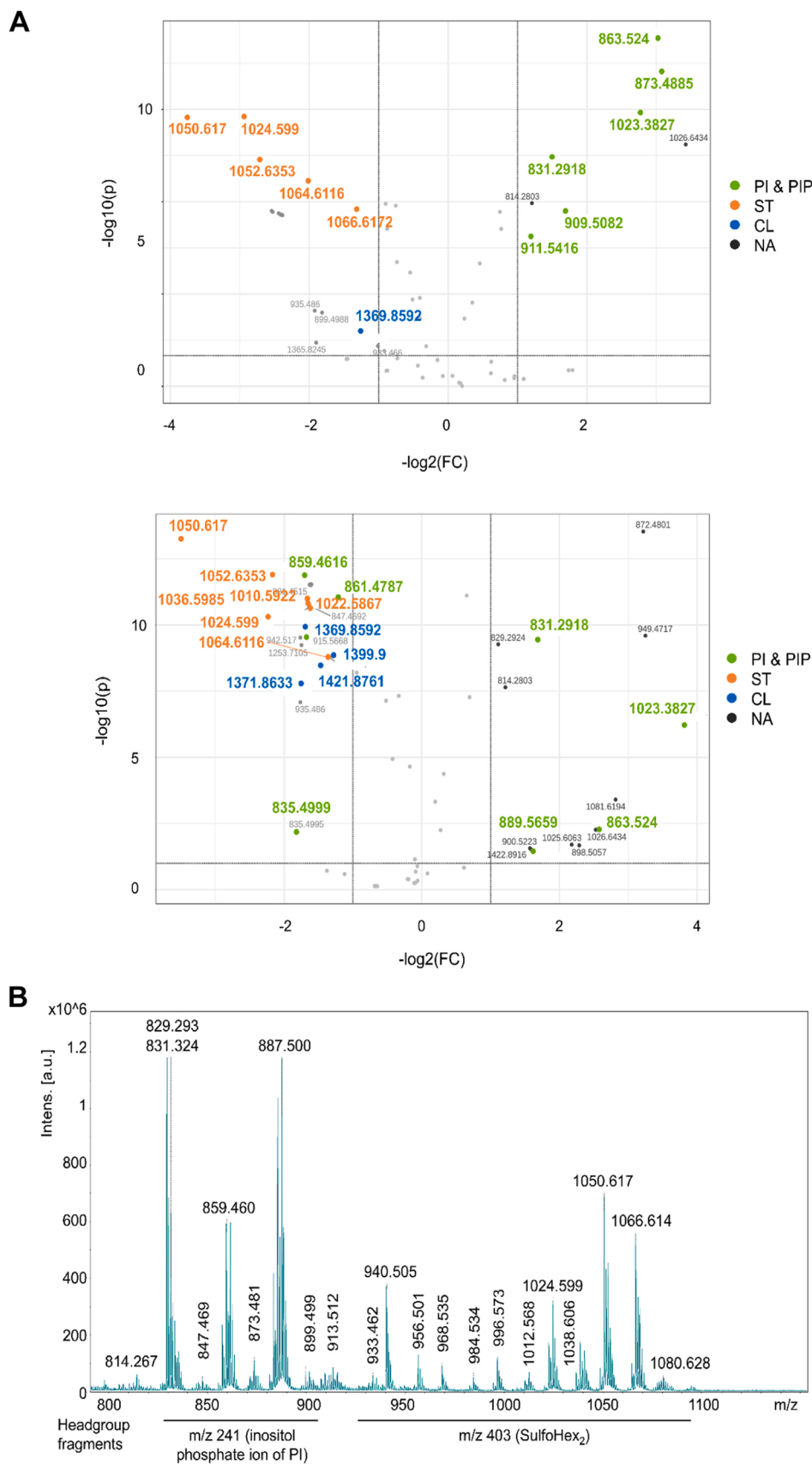
We also quantified the average fluorescence intensity derived from MitoTracker Deep Red in 50 cells from each group (control and 7-day DFO-treated). We compared the average fluorescence intensity of the control group to that of the 7-day DFO-treated group and found that it was significantly higher in the control group (p < 0.0001). This is consistent with the notion that mitochondria become damaged and dysfunctional after DFO treatment, as MitoTracker Deep Red stains active mitochondria.

Impaired mitochondria are targeted by the autophagic system to be delivered to lysosomes, where they are degraded in a process called mitophagy (Onishi et al., 2021). A common indicator of mitochondrial damage is the externalization of CLs to the mitochondrial outer membrane. CL externalization triggers mitophagy by signaling for the binding of the autophagy-related protein LC3B (Iriondo et al., 2022). Mitophagy is also induced by hypoxia, reducing the number of mitochondria to shift the cell metabolism towards the anaerobic pathway (Onishi et al., 2021). Given that DFO causes mitochondrial damage and induces hypoxia (Al Tameemi et al., 2019) and we observed an increase in the expression of LC3B by HepG2 cells after DFO treatment (Fig. 2B and D), we investigated mitophagy via fluorescent staining of mitochondria and LC3B. We observed increased levels of LC3B, but mitochondria and LC3B did not co-localize (Fig. 3C); we quantified the co-localization between LC3B and mitochondria using the ImageJ Plugin JACoP and evaluated the Pearson's coefficient R for 50 cells from the treated group and 50 cells from the control group. The average R was < 0.3 for both treated and untreated cells, indicating no significant
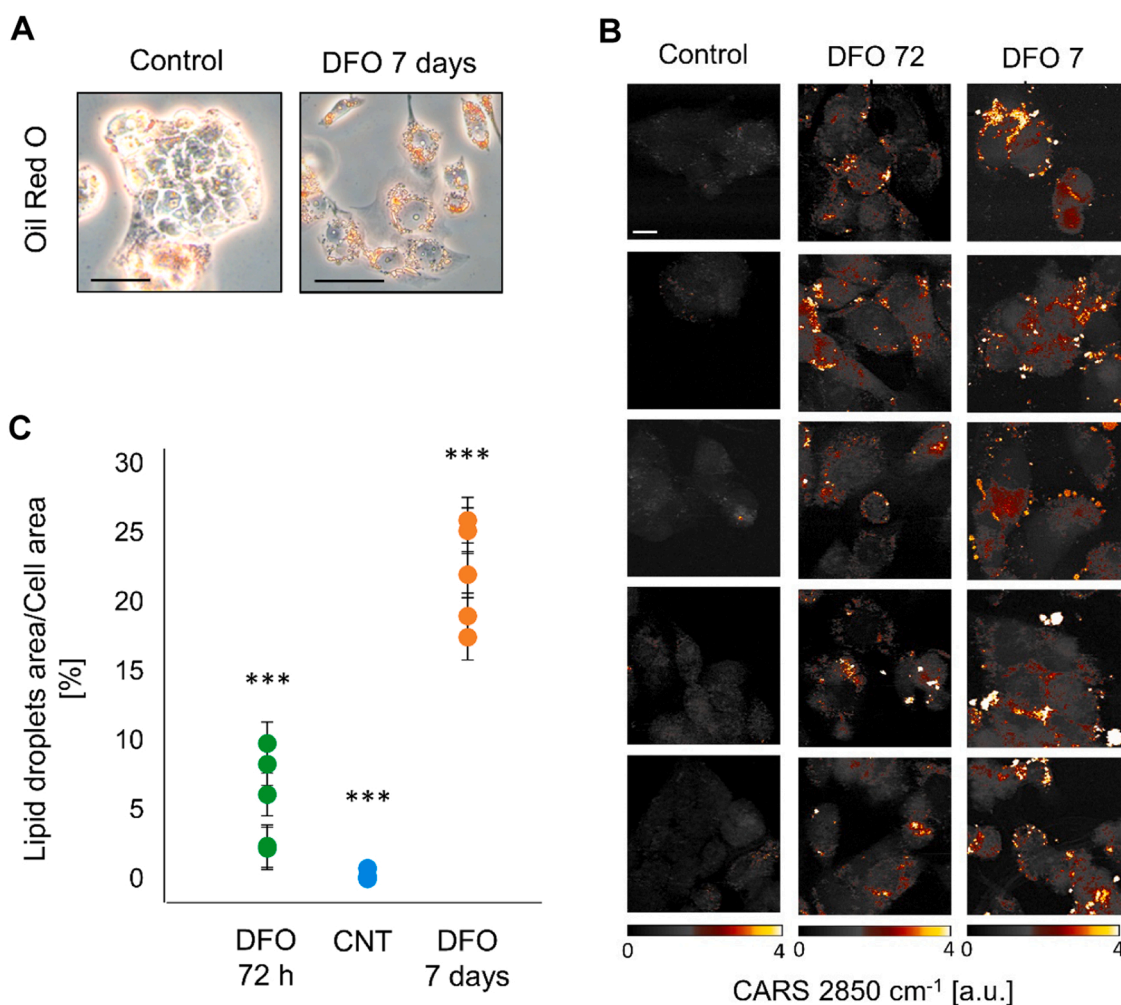


**Fig. 4.** DFO induces an increase in lipid droplet size. **(A)** Lipid droplets within control and 7-day DFO-treated HepG2 cells stained with Oil Red O. Cells were observed and imaged using an optical microscope. Scale bar = 50 μm. **(B)** CARS images of lipid droplets within control cells and 72 h and 7-day DFO-treated HepG2 cells. Scale bar = 10 μm. **(C)** Dot plot showing the percentage of lipid droplet area/cell area and lipid droplet concentrations (a.u.) in control vs. 72 h and 7-day DFO-treated HepG2 cells imaged using CARS. For % lipid droplets area/cell area: raw CARS images at 2850 cm$^{-1}$ were thresholded, and then the area above the threshold was normalized over the total cell area (from relative light transmission images). The threshold was the same for all control and DFO cells and was chosen to distinguish lipid accumulations from the cytosol signal. p = 0.01 with U-Mann Whitney test. For lipid droplet concentrations: raw CARS images at 2850 cm$^{-1}$ were thresholded, and then the square root of the mean CARS signal above the threshold was computed, which is linearly proportional to the concentration of lipid droplets in the focal volume. The threshold was the same for all control and DFO cells and was chosen to distinguish lipid accumulations form the cytosol signal (p > 0.05, U-Mann Whitney test).

**A**



**Fig. 5.** MALDI analysis of lipid extracts from HepG2 cells. **(A)** Volcano plots of changes in molecular species of lipids from control vs. 72 h (upper panel) and 7-day (lower panel) DFO-treated HepG2 cells. Grey values show lipid species with non-significant changes. Negative values (to the left) indicate upregulated lipid species in control samples ($p < 0.05$), whereas positive values (to the right) reflect downregulated lipids in control samples ($p < 0.05$). $-\log10$ p $= -\log10$ nominal P-value; $\log2FC = \log2$ fold changes. Lipids are colored according to the species, NA (not available) indicates lipid species that were not identified. **(B)** Magnification of *m/z* 800–1100 range acquired in negative-ion mode, including PI and ST regions (*m/z* 900–1100) indicated by bars.

**B**

co-localization of LC3B and lysosomes. This suggests that mitochondria, although damaged, were not eliminated through autophagy. This is consistent with the reported impairment of mitophagy in senescent cells (Chapman et al., 2019; Korolchuk et al., 2017).

*3.4. DFO treatment induces an increase in the number and size of lipid droplets*

Mitochondrial involvement in lipogenesis and triacylglyceride synthesis, and consequently LD formation, is well known (Benador et al.,
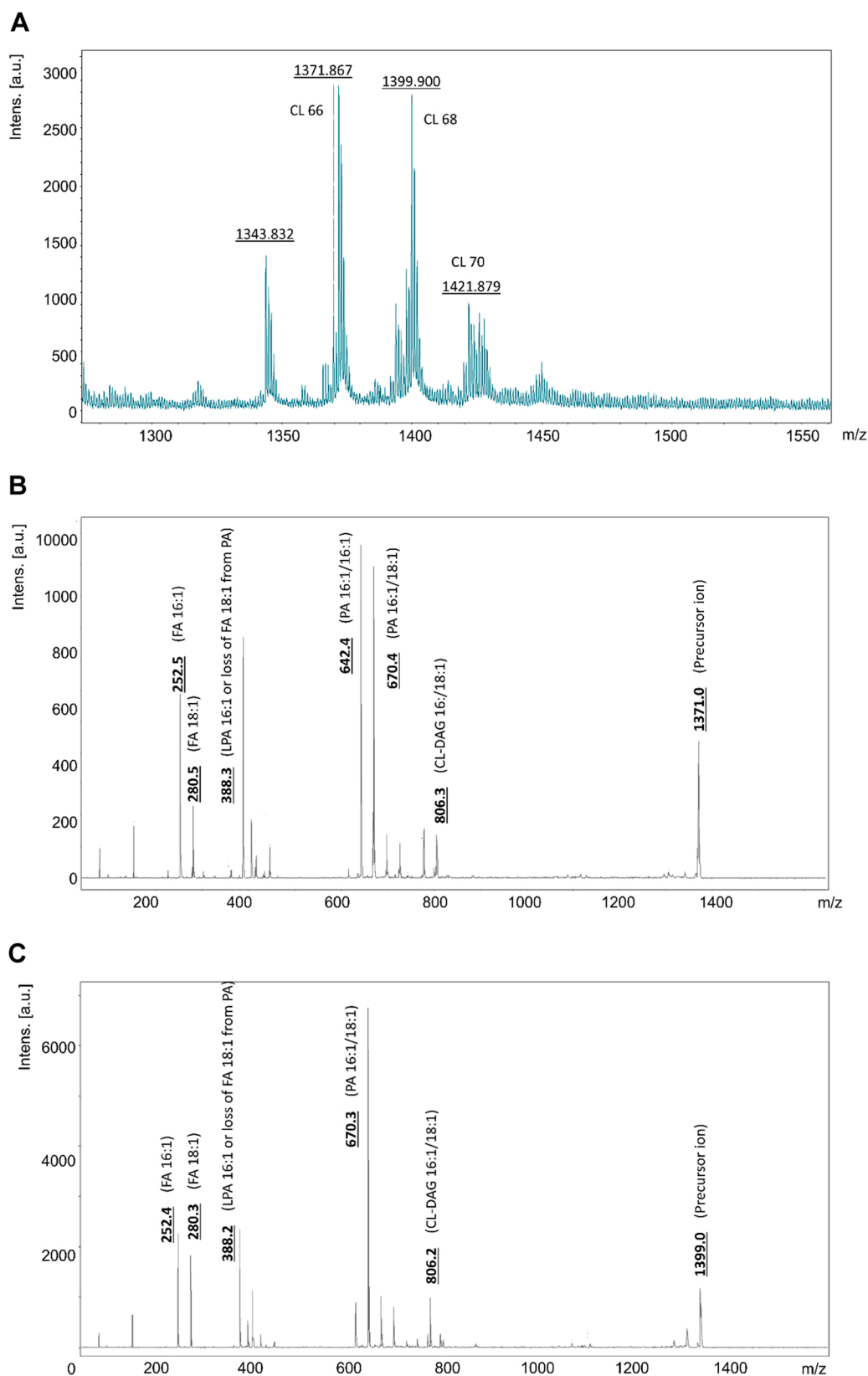


**Fig. 6.** Magnification of the *m/z* 1300–1500 range acquired in negative-ion mode including CL species and relative identification using the LIFT method. **(A)** The species of CLs with the same acyl chain length were categorized in groups. CLs in HepG2 cells had three major groups: CL66, CL68, CL70. **(B)** Product ion spectra obtained from MS/MS of *m/z* 1371.0 (Δppm −51) in negative ion mode. Key product ion structures with corresponding *m/z* are shown. In addition to characteristic product ions of fatty acids, such as FA 16:1 (*m/z* 252.5) and FA 18:1 (*m/z* 280.5), fragments of the phosphatidyl part (PA) of CL gave information about the FA combination. In this case, the prevailing fragments *m/z* 642.4 (PA 16:1_16:1) and 670.4 (PA 16:1_18:1) are characteristic of CL 66:4. The peak at *m/z* 388.3 represents loss of FA 18:1 from the sn-2 position of the 16:1_18:1 PA structure. The fragmentation pattern is consistent with the structure 16:1_16:1/16:1_18:1. **(C)** Product ion spectra obtained from MS/MS of *m/z* 1399.0 (Δppm −42) in negative ion mode. Key product ion structures with corresponding *m/z* are shown. In addition to characteristic product ions of fatty acids, such as FA 16:1 (*m/z* 252.4) and FA 18:1 (*m/z* 280.3), fragments of the phosphatidyl part (PA) of CL gave information about the FA combination. In this case, the prevailing fragments *m/z* 670.3 and 806.2 are characteristic of CL 68:4 with the combination of FA 16:1 and FA 18:1 (PA 16:1_18:1) and diacylglyceride (DAG) moiety 16:1_18:1, respectively. The peak at *m/z* 388.2 represents loss of FA 18:1 from the sn-2 position of the 16:1_18:1 PA structure. The fragmentation pattern is consistent with the structure 16:1_18:1/16:1_18:1.

2019). Therefore, we next asked whether DFO-induced mitochondrial damage affected the amount and size of LDs within HepG2 cells. We stained untreated and 7-day DFO-treated HepG2 cells with Oil Red O. Upon DFO treatment, LDs appeared to be increased in both number and size, with heterogeneous dimensions (Fig. 4A). As Oil Red O staining did not make it clear whether LDs became bigger and more numerous or simply became more visible as the cells lost their compact structure, we measured the size and concentration of LDs within control cells and 72 h and 7-day DFO-treated HepG2 cells using CARS (Fig. 4B). When matching the 2850 cm$^{-1}$ Raman mode of lipids, CARS images revealed a significant increase in the cell area containing LDs in DFO-treated HepG2 cells compared to controls (Fig. 4 C, p = 0.01 with two-sided U-Mann Whitney test, Fig. 4B-C).

### 3.5. DFO treatment causes deep remodeling of the lipid profile of surviving cells

As phospholipids (PLs) play different roles in senescence (Hamsanathan and Gurkar, 2022), we investigated major PLs from untreated cells and 72 h or 7-day DFO-treated HepG2 cells and compared their profiles using MALDI-MS. The mass spectra were acquired in negative-ion mode. Following DFO treatment, important changes were evident in the relative peak intensities (Supplementary File 2, Fig. S1). A volcano plot was used to identify significant $m/z$ values with an increased or decreased fold change (Fig. 5A). The signals in the PI region ($m/z$ 800–900) changed modestly (Fig. 5B), but those related to regions $m/z$ 900–1100 and $m/z$ 1300–1500 underwent a considerable decrease after treatment with DFO. Main peaks were identified by MS/MS analysis using the LIFT method and LIPID MAPS structure database. PIs were identified using the headgroup fragments $m/z$ 223, 241, and 259, with the main being $m/z$ 241. Species PI 34:1, PI 36:1, and PI 38:4 were the predominant PI species (Fig. 5B).

Spectra from DFO-treated cells showed evident changes in the cluster of peaks with $m/z$ 940.5, 956.5, 968.5, 984.5, 996.6, 1012.6, 1024.6, 1038.6, 1050.6, and 1066.6. Striking differences were noted in the region of CLs, including a cluster of peaks observed at $m/z$ 1343.8, 1369.8, 1371.9, 1399.9, and 1421.9. Because we had observed an alteration of the mitochondria network (Section 3.3), CL changes were expected. Using the LIFT method, we tentatively identified several ST species in the $m/z$ 900–1100 region and in the CL region at $m/z$ 1300–1500 (Fig. 6A). Examples of CL identification are shown in Fig. 6B and C. ST fragmentation was characterized by three dominant ions ($m/z$ 97, 241, and 403), all corresponding to common ion peaks of ST molecular species derived from the sulfation of lactosylceramide (LacCer, Hex$_2$Cer,

where Hex is used to indicate Glc and Gal that cannot be differentiated using MS). A sulfate group is attached to the C3-hydroxyl of galactose, generating sulfatide species (SHexCer and SHex$_2$Cer) (Hsu and Turk, 2008). The CL fragmentation pattern of molecular ions at $m/z$ 1371.9 and $m/z$ 1399.9 corresponded to CL 66:4 and CL 68:4 (Chen et al., 2017).

We carried out statistical analyses by comparing the spectra of control and DFO-treated samples using MetaboAnalyst software (Supplementary File 1). Fig. 7A shows the supervised PLS-DA, which was applied to obtain information on changes in the $m/z$ values due to DFO treatment: control and DFO spectra were well separated in a 2D score plot and the observed differences among the control and DFO groups exceeded the observed variability between the replicates. Notably, the duration of treatment imparted coherent changes to the HepG2 lipidome. The hierarchical clustering heatmap of the normalized data (Fig. 7B) clearly showed that samples treated with DFO were characterized by large changes in peak intensity. Exploring the self-organizing map (SOM) of sample-related $m/z$ values, we found that 72 h DFO-treated samples and 7-day DFO-treated samples clustered together distant to control samples (Supplementary File 2, Fig. S2), further showing that temporal changes in DFO treatment produced broad similar effects on the cells. Furthermore, as HepG2 cells were clearly senescent after 7 days of treatment, DFO-mediated changes may be considered relevant for the pathobiology of HepG2 senescence.

### 3.6. Direct analysis of phospholipids in HepG2 cellular spheroids

MALDI-MSI was used to analyze changes in the spatial distribution of lipid species in HepG2 spheroid-like structures with or without 72 h of DFO exposure. In particular, we were interested in investigating whether the spatial distribution of PI, ST, and CL ions could be associated with features of DFO-induced cellular senescence. Ion distribution images of control and DFO-treated samples seeded on ITO slides were acquired with an UltrafleXtreme TOF/TOF mass spectrometer using negative ion mode. The peak identities mentioned in Section 3.5 were further confirmed by in situ MALDI MS/MS with the support of the LIPID MAPS structure database (data not shown). Imaging spectra showed marked differences induced by DFO treatment in the distribution of the lipid species in accordance with the data obtained in experiments on solubilized cellular preparations. Fig. 8 shows optical (A) and MS images (B-D) of HepG2 spheroids with or without DFO treatment. MSI reflects the distribution of some previously identified PI, ST, and CL molecular species. Specifically, ion images for $m/z$ 885.1 (PI 38:4), $m/z$ 909.1 (PI 40:6), $m/z$ 861.2 (PI 36:1), $m/z$ 1036.2 (SHex$_2$Cer 41:2), $m/z$ 1052.4
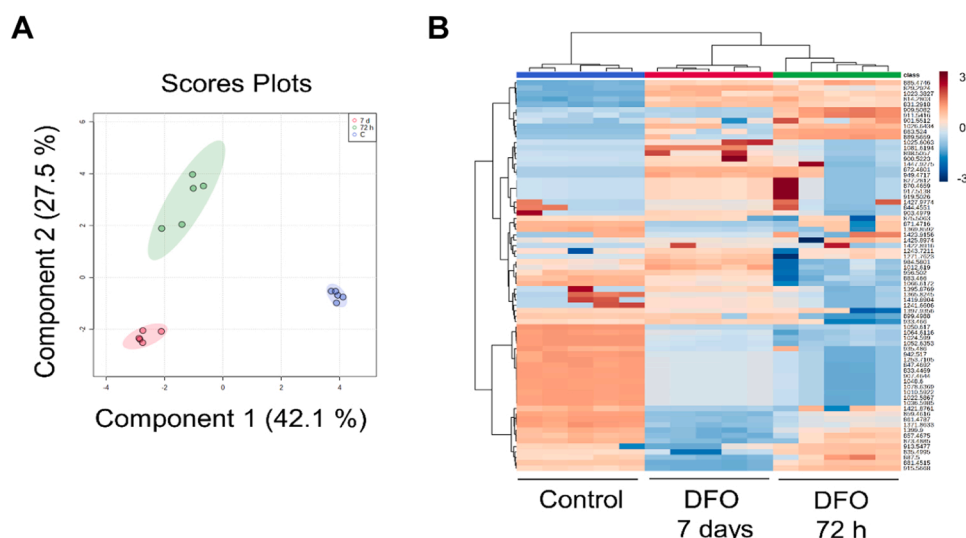


**Fig. 7.** Lipid features of DFO-treated HepG2 cells and controls. **(A)** PLS-DA score plots of the top most differential lipid-related $m/z$ values obtained by the PLS-DA utility of MetaboAnalyst software for control HepG2 cells (blue) and 72 h (green) and 7-day DFO-treated cells (red). The ellipses showing the 95% confidence limits of a normal distribution for each spectra group (N = 5) have been marked in the respective colors. PLS-DA was applied to the log-transformed and Pareto scaled dataset. **(B)** Hierarchical clustering (heatmap) was performed on the normalized data (distance measured using Euclidean and clustering algorithm using Complete). Each colored cell on the map corresponds to an $m/z$ intensity value, with samples in columns and $m/z$ values in rows.
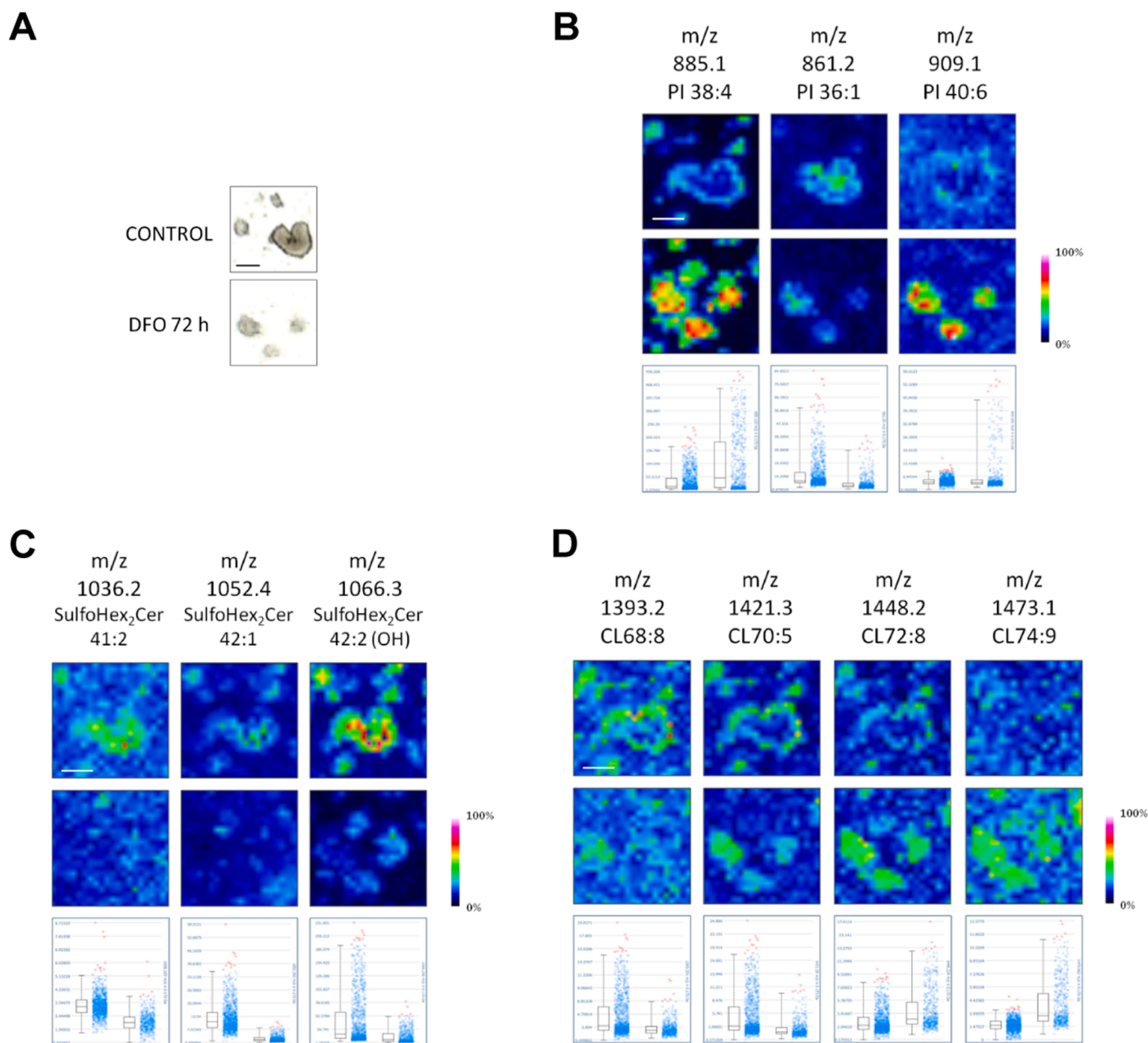
**Fig. 8.** Imaging of lipids using MALDI. Untreated and 72 h DFO-treated HepG2 cells were seeded on an ITO slide and imaged by MALDI-TOF in negative ion mode (spatial resolution: 50 μm). **(A)** TIFF images of HepG2 spheroids on the ITO slide taken prior to 9AA matrix application. **(B)** Distribution of PIs (*m/z*: 885.1, 861.2, and 909.1) with relative density plots showing the median intensities. Blue dots represent the spectra in which the intensities of the given *m/z* interval are between the lower and upper quartiles, and red dots represent outliers. **(C)** Average mass spectrum of representative SHex$_2$Cer species (*m/z*: 1036.2, 1052.4, 1066.3). **(D)** CLs (*m/z* 1393.2, 1421.2, 1448.2, 1473.1). Total ion current (TIC) normalization was used. Color bars: 0–100% relative intensity. Scale bar = 500 μm.

(SHex$_2$Cer 42:1), *m/z* 1066.3 (SHex$_2$Cer 42:2 OH), *m/z* 1421.3 (CL 70), *m/z* 1448.2 (CL 72), and *m/z* 1473.01 (CL 74). The signal intensity derived from arachidonyl (20:4 fatty acyl)-containing PI 38:4 (18:0–20:4) in untreated HepG2 spheroids was faint compared to that of DFO-treated spheroids, likely revealing an elevated intensity in the central (possibly hypoxic) regions of the spheroids. Overall, MALDI imaging analysis strongly supported the MALDI-MS data from solubilized cellular preparations.

## 4. Discussion

We showed that, in addition to causing cell death, DFO induced a senescence-like cell cycle arrest in HepG2 cells, a hepatocellular carcinoma-derived cell line widely used to investigate drug-induced metabolic perturbations. In our experiments, especially after 7 days of treatment, we noted cells with increased cell size, enhanced β-gal activity, mitochondria elongation, and DNA damage response activation, all well-known features of senescent cells. A likely explanation supported by previous data is that DFO sequestered iron inside lysosomes, leading to iron deficiency (Kurz et al., 2006). As DNA polymerases requires iron to function properly, the lack of it impacts DNA replication (Puig et al., 2017), activating the DNA damage response, including DNA replication arrest (Ciccia and Elledge, 2010; Puig et al., 2017).

Iron depletion also causes mitochondrial dysfunction and impaired mitophagy, preventing mitochondrial renewal through selective degradation, which is also a common feature of cellular senescence. Mitophagy plays a central role in mitochondria dynamics (fusion and fission), which are linked to mitochondrial morphology, which itself is tightly associated with the energetic status of the cell (Picard et al., 2013). Elongation of mitochondria, as we observed in our model, may

reflect an abnormal distribution or partial loss of cristae, which are accompanied by a decrease in the inner membrane potential and oxygen consumption, lower ATP levels, and inhibition of cell proliferation (Sabouny and Shutt, 2020). Accordingly, mitochondrial elongation has been ascertained to be sufficient for developing a senescent phenotype with increased ROS production (Yoon et al., 2006). These modifications could correspond to the metabolic needs of senescent cells or reflect respiratory chain deficiency and explain the observation of abundant accumulation of lipids in droplets.

Using MALDI-MS and MALDI-MSI, we found significant differences in CL profiles as an effect of DFO treatment. CLs are the signature lipids of mitochondria and have a plethora of functions, including maintenance of cristae morphology, mitochondrial dynamics, and electron transport chain super complex formation. Alterations in the CL profile may negatively impact the activity of a variety of mitochondrial proteins and enzymes, including the electron transport chain and OXPHOS complexes, contributing to the impairment in mitochondrial function and dynamics (Chapman et al., 2019).

In addition to remodeling of the CL profile, we detected significant changes in the profiles of PIs following treatment with DFO, especially at 7 days, when the senescence phenotype was fully developed. MSI analysis revealed that the amount of PI (18:0_20:4) increased in the inner region of HepG2 spheroid-like structures after DFO treatment. C20:4 is a precursor of inflammatory molecules widely reported in senescent cells (Xie et al., 2016).

PIs also have highly specialized roles in cells. Phosphorylated derivatives play major roles in signal transduction, membrane trafficking, and maintenance of the actin cytoskeletal network. The synthesis of both PI and CL species requires cytidine diphosphate diacylglycerol (CDP-DAG). CDP-DAG is synthesized from phosphatidic acid (PA) and citidine triphosphate (CTP) (Blunsom and Cockcroft, 2020). PI synthesis occurs at the endoplasmic reticulum, whereas CLs are synthesized in the mitochondria. The generalized decrease we observed for both PI and CL species after DFO treatment suggests a limited availability of precursors and/or impaired activity of enzymes involved in lipid biosynthesis during the establishment and maintenance of senescence.

Despite a reduction in the intensities of many lipid species, we observed LD accumulation within HepG2 cells. An explanation is that PA can be redirected to generate diacylglycerol and triacylglycerol (TAG) instead of being utilized for the synthesis of CDP-DAG (Blunsom and Cockcroft, 2020). TAG is mainly used for storing excess fatty acids. These molecules are deposited within LDs and provide building blocks for membranes or substrates for energy metabolism (Millner and Atilla-Gokcumen, 2020; Olzmann and Carvalho, 2019). The accumulation of LDs is also thought to play a protective role during senescence. TAG sequestration in LDs, especially species containing unsaturated fatty acids that are prone to oxidation and forming lipid peroxides, may limit membrane damage under oxidative stress during senescence (Millner and Atilla-Gokcumen, 2020).

Glycosphingolipid sulfates or sulfatides were highly represented in untreated HepG2 cells. They are strongly reduced by DFO treatment: they derive from the sulfation of galactosylceramide species (sulfoHexCer) and contain the monosulfated lactosilic moiety (sulfoHex2Cer) (Czumaj and Śledziński, 2020). Uridine diphosphate (UDP)-glucose ceramide glucosyltransferase (UGCG) catalyzes the first glycosylation step in the synthesis of glycosphingolipids (GSLs). By transferring UDP-glucose to ceramide, glucosylceramide (GlcCer, cerebroside) is produced, which is the precursor for all complex GSLs. UGCG, which resides in the Golgi apparatus, is the key enzyme of GSL metabolism. Sulfatides carry a sulfate ester group, which is attached to the carbohydrate moiety by galactosylceramide sulfotransferase (GAL3ST1). Diversity of sulfatide molecular species refers to sugar moieties and ceramide moieties, which are probably important for peculiar effective functions in specific microenvironments, such as lipid membrane microdomains or lipid rafts, by regulating interactions between neighboring proteins and lipids (Kyogashima et al., 2006; Zellhofer and Beukelman, 1992).

Levels of sulfatides are generally elevated in colorectal, ovarian, or renal carcinoma (Jirásko et al., 2022) and intrahepatic cholangiocarcinoma (Huizing et al., 2023). Sulfatides are often elevated in hepatocellular carcinma (HCC) (Takahashi and Suzuki, 2012), and previous studies have shown that sulfatides are promoters of cell adhesion and metastasis in HCC (Wang et al., 2016). The elevated sulfatide content of HCC cells has been found to activate clustering and phosphorylation of integrin αVβ3 accelerating cell growth in HCC independent on ECM ligand binding. (Wang et al., 2016). Enhanced synthesis of sulfatides through overexpression of GAL3ST1 results in an increased metastatic potential of tumor cells (Suchanski et al., 2018).

Chemotherapy promotes the generation of ceramide through a *de novo* synthesis response, and ceramide is a master promoter of apoptotic processes (Dany and Ogretmen, 2015). Danuorubicin, etoposide, camptothecin, and gemcitibine appear to cause *de novo* ceramide biosynthesis either by activation of dihydroceramide synthases or by increasing the activity of serine palmitoyl transferase, the first step in the *de novo* pathway (Bose et al., 1995, Chalfant et al., 2002, Chauvier et al., 2002, Perry et al., 2000). Inhibiting the *de novo* pathway of ceramide synthesis antagonizes the cytotoxic effects of *de novo* ceramide generation and the synthesis of sulfatides. The ceramide biosynthesis pathway is catalyzed by dihydroceramide desaturase (DES1) in most tissues and DES2 in the intestines, kidneys, and skin. These enzymes that have two oxygen atoms in their active site, forming a complex with two iron ions, and a connection between hypoxia or oxidative stress and the accumulation of dihydroceramide precursors of ceramide species has been demonstrated (Zelnik et al., 2020). Therefore, ceramide metabolism and iron regulation are mechanistically linked. As ceramide is a premetabolite of sulfatides, reduction of the sulfatide content may be a signal of DES1/DES2 inhibition. We observed a significant decrease in the levels of SulfoHexCer and SulfoHex$_2$Cer species in DFO-treated cells.

An accumulation of dihydroceramide has been reported to impair autophagic flux and increase TG storage in LDs in a hepatic steatosis model (Lee et al., 2017; Torti and Torti, 2013). In addition to observing an increase of LDs, we found an increased level of LC3B or accumulation puncta with blockade of autophagosome formation and changes in mitochondrial dysfunction, often due to a related reduction in mitophagy (Zhang et al., 2013). Our results support the view that DFO acts in HepG2 cells to produce oxidative stress-induced senescence via sequential mitochondrial and lysosomal dysfunction (Tai et al., 2017).

In some cases, sulfatides may act as pro-apoptotic molecules, making cancer cells more prone to environmental stressors, such as hypoxia and anticancer drugs (Giussani et al., 2014). Thus, we cannot exclude the possibility that HepG2 cells highly expressing ceramide and sulfatides are mostly susceptive to apoptosis. However, elevated sulfatide content requires specific enzymatic activities downstream of ceramide biosynthesis. Notably, sulfatide species are more abundant in raft membranes, where interactions with proteins regulate signaling and adhesive processes. We are inclined to assume that high sulfatide content in HepG2 cells interferes with propagation of the death pathways and supports the peculiarly high rate of growth of these cells. It could be that those HepG2 cells that undergo senescence do not necessitate sulfatide-mediated signaling.

Further research is required to address the role of sulfatides in tumor growth, proliferation, senescence, and the possibility of modulating sulfatide metabolism for a potential therapeutic purpose. By stimulating ceramide or inhibiting catabolic enzymes, such as UGCG, we could understand whether there is a link between the lower expression of SHex$_2$Cer species and DFO-mediated senescence in HepG2 cells.

In conclusion, DFO leads to drastic changes in the cellular lipids of HepG2 cells that survive DFO treatment and develop a senescent phenotype. The proliferation-senescence switch was strongly associated with a marked remodeling of PI, sulfatide, and CL species, which play a central and general role in cell signaling cascades, intracellular membrane trafficking, and mitochondrial functions. However, the precise mechanisms involved have not yet been fully deciphered, mainly due to

the complexity of the modifications.

This work has some limitations. Our studies are beginning to reveal specific sub-classes and species of sulfatides that change in iron-depleted conditions. Further investigation is needed to better understand this interplay and the role of senescence and iron depletion in cancer cells. Enzyme activities and pre-metabolites that generate them should be analyzed to generate complete information that is therapeutically useful. Another caveat of this study is that the TAG species were not measured. We do not know if uptake or biosynthesis was underlying the lipid accumulation, presumably of TAG, in LDs.

## Funding sources

## CRediT authorship contribution statement

**Silvia Ghislanzoni:** Conceptualization, Data curation, Formal analysis, Investigation, Methodology, Visualization, Writing – original draft, Writing – review & editing. **Gaia Martina Sarcinelli:** Data curation, Formal analysis, Investigation, Methodology, Visualization, Writing – original draft, Writing – review & editing. **Arianna Bresci:** Conceptualization, Formal analysis, Investigation, Methodology, Visualization, Writing – original draft. **Francesco Manetti:** Investigation. **Dario Polli:** Funding acquisition, Supervision. **Antonella Tomassetti:** Resources, Writing – review & editing. **Maria Teresa Radice:** Methodology. **Italia Bongarzone:** Conceptualization, Formal analysis, Funding acquisition, Investigation, Project administration, Resources, Supervision, Writing – original draft, Writing – review & editing.

## Declaration of Competing Interest

The authors declare no conflict of interest.

## Data Availability

Data will be made available on request. All analyses relevant to the study were included in the article or uploaded as Supplementary Information.

## Appendix A. Supporting information

Supplementary data associated with this article can be found in the online version at doi:10.1016/j.biocel.2023.106419.

## References

Al Tameemi, W., Dale, T.P., Al-Jumaily, R.M.K., Forsyth, N.R., 2019. Hypoxia-modified cancer cell metabolism. Front. Cell Dev. Biol. 7, 4.

Benador, I.Y., Veliova, M., Liesa, M., Shirihai, O.S., 2019. Mitochondria bound to lipid droplets: where mitochondrial dynamics regulate lipid storage and utilization. Cell Metab. 29, 827–835.

Bose, R., Verheij, M., Haimovitz-Friedman, A., Scotto, K., Fuks, Z., Kolesnick, R., 1995. Ceramide synthase mediates daunorubicin-induced apoptosis: an alternative mechanism for generating death signals. Cell 82 (3), 405–414.

Breil, C., Abert Vian, M., Zemb, T., Kunz, W., Chemat, F., 2017. "Bligh and Dyer" and folch methods for solid-liquid-liquid extraction of lipids from microorganisms. Comprehension of solvatation mechanisms and towards substitution with alternative solvents. Int. J. Mol. Sci. 18, E708.

Chalfant, C.E., Rathman, K., Pinkerman, R.L., Wood, R.E., Obeid, L.M., Ogretmen, B., Hannun, Y.A., 2002. De novo ceramide regulates the alternative splicing of caspase 9 and Bcl-x in A549 lung adenocarcinoma cells. Dependence on protein phosphatase-1. J Biol Chem 277 (15), 12587–12595.

Chapman, J., Fielder, E., Passos, J.F., 2019. Mitochondrial dysfunction and cell senescence: deciphering a complex relationship. FEBS Lett. 593, 1566–1579.

Chaston, T.B., Richardson, D.R., 2003. Iron chelators for the treatment of iron overload disease: relationship between structure, redox activity, and toxicity. Am. J. Hematol. 73, 200–210.

Chen, Z., Wu, Y., Ma, Y.-S., Kobayashi, Y., Zhao, Y.-Y., Miura, Y., Chiba, H., Hui, S.-P., 2017. Profiling of cardiolipins and their hydroperoxides in HepG2 cells by LC/MS. Anal. Bioanal. Chem. 409, 5735–5745.

Ciccia, A., Elledge, S.J., 2010. The DNA damage response: making it safe to play with knives. Mol Cell. 40 (2), 179–204.

Dany, M., Ogretmen, B., 2015. Ceramide induced mitophagy and tumor suppression. Biochim. Biophys. Acta 1853, 2834–2845.

De Bortoli, M., Taverna, E., Maffioli, E., Casalini, P., Crisafi, F., Kumar, V., Caccia, C., Polli, D., Tedeschi, G., Bongarzone, I., 2018. Lipid accumulation in human breast cancer cells injured by iron depletors. J. Exp. Clin. Cancer Res. 37, 75.

Donfrancesco, A., Deb, G., Dominici, C., Pileggi, D., Castello, M.A., Helson, L., 1990. Effects of a single course of deferoxamine in neuroblastoma patients. Cancer Res. 50, 4929–4930.

Estrov, Z., Tawa, A., Wang, X.H., Dubé, I.D., Sulh, H., Cohen, A., Gelfand, E.W., Freedman, M.H., 1987. In vitro and in vivo effects of deferoxamine in neonatal acute leukemia. Blood 69, 757–761.

Garciaz, S., Guirguis, A.A., Müller, S., Brown, F.C., Chan, Y.-C., Motazedian, A., Rowe, C. L., Kuzich, J.A., Chan, K.L., Tran, K., Smith, L., MacPherson, L., Liddicoat, B., Lam, E. Y.N., Cañeque, T., Burr, M.L., Litalien, V., Pomilio, G., Poplineau, M., Duprez, E., Dawson, S.-J., Ramm, G., Cox, A.G., Brown, K.K., Huang, D.C.S., Wei, A.H., McArthur, K., Rodriguez, R., Dawson, M.A., 2022. Pharmacologic reduction of mitochondrial iron triggers a noncanonical BAX/BAK-dependent cell death. Cancer Discov. 12, 774–791.

Gilazieva, Z., Ponomarev, A., Rutland, C., Rizvanov, A., Solovyeva, V., 2020. Promising applications of tumor spheroids and organoids for personalized medicine. Cancers 12.

Giussani, P., Tringali, C., Riboni, L., Viani, P., Venerando, B., 2014. Sphingolipids: key regulators of apoptosis and pivotal players in cancer drug resistance. Int. J. Mol. Sci. 15, 4356–4392.

Gorgoulis, V., Adams, P.D., Alimonti, A., Bennett, D.C., Bischof, O., Bishop, C., Campisi, J., Collado, M., Evangelou, K., Ferbeyre, G., Gil, J., Hara, E., Krizhanovsky, V., Jurk, D., Maier, A.B., Narita, M., Niedernhofer, L., Passos, J.F., Robbins, P.D., Schmitt, C.A., Sedivy, J., Vougas, K., von Zglinicki, T., Zhou, D., Serrano, M., Demaria, M., 2019. Cellular senescence: defining a path forward. Cell 179, 813–827.

Hamsanathan, S., Gurkar, A.U., 2022. Lipids as regulators of cellular senescence. Front. Physiol. 13, 796850.

Heath, J.L., Weiss, J.M., Lavau, C.P., Wechsler, D.S., 2013. Iron deprivation in cancer–potential therapeutic implications. Nutrients 5, 2836–2859.

Hentze, M.W., Muckenthaler, M.U., Andrews, N.C., 2004. Balancing acts: molecular control of mammalian iron metabolism. Cell 117, 285–297.

Hsu, F.-F., Turk, J., 2008. Structural characterization of unsaturated glycerophospholipids by multiple-stage linear ion-trap mass spectrometry with electrospray ionization. J. Am. Soc. Mass Spectrom. 19, 1681–1691.

Huizing, L., Chen, L., Roeth, A.A., Heij, L.R., Flinders, B., Bouwense, S.A.W., Balluff, B., Neumann, U.P., Heeren, R.M.A., Olde Damink, S.W.M., Vreeken, R.J., Schaap, F.G., 2023. Tumor ratio of unsaturated to saturated sulfatide species is associated with disease-free survival in intrahepatic cholangiocarcinoma. Cell Oncol.

Iriondo, M.N., Etxaniz, A., Varela, Y.R., Ballesteros, U., Hervás, J.H., Montes, L.R., Goñi, F.M., Alonso, A., 2022. LC3 subfamily in cardiolipin-mediated mitophagy: a comparison of the LC3A, LC3B and LC3C homologs. Autophagy 1–19.

Jirásko, R., Idkowiak, J., Wolrab, D., Kvasnička, A., Friedecký, D., Polański, K., Študentová, H., Študent, V., Melichar, B., Holčapek, M., 2022. Altered plasma, urine, and tissue profiles of sulfatides and sphingomyelins in patients with renal cell carcinoma (preprint). Oncology.

Korolchuk, V.I., Miwa, S., Carroll, B., von Zglinicki, T., 2017. Mitochondria in Cell Senescence: Is Mitophagy the Weakest Link? EBioMedicine 21, 7–13.

Kurz, T., Bertil Gustafsson, B., Brunk, U.T., 2006. Intralysosomal iron chelation protects against oxidative stress-induced cellular damage. FEBS J. 273 (13), 3106–3117.

Kyogashima, M., Tamiya-Koizumi, K., Ehara, T., Li, G., Hu, R., Hara, A., Aoyama, T., Kannagi, R., 2006. Rapid demonstration of diversity of sulfatide molecular species from biological materials by MALDI-TOF MS. Glycobiology 16, 719–728.

Lee, A.Y., Lee, J.W., Kim, J.-E., Mock, H.J., Park, S., Kim, S., Hong, S.-H., Kim, J.-Y., Park, E.-J., Kang, K.-S., Kim, K.P., Cho, M.-H., 2017. Dihydroceramide is a key metabolite that regulates autophagy and promotes fibrosis in hepatic steatosis model. Biochem. Biophys. Res. Commun. 494, 460–469.

Lee, B.Y., Han, J.A., Im, J.S., Morrone, A., Johung, K., Goodwin, E.C., Kleijer, W.J., DiMaio, D., Hwang, E.S., 2006. Senescence-associated beta-galactosidase is lysosomal beta-galactosidase. Aging Cell 5, 187–195.

Lu, F.-K., Basu, S., Igras, V., Hoang, M.P., Ji, M., Fu, D., Holtom, G.R., Neel, V.A., Freudiger, C.W., Fisher, D.E., Xie, X.S., 2015. Label-free DNA imaging in vivo with stimulated Raman scattering microscopy. Proc. Natl. Acad. Sci. USA 112, 11624–11629.

Mah, L.-J., El-Osta, A., Karagiannis, T.C., 2010. gammaH2AX: a sensitive molecular marker of DNA damage and repair. Leukemia 24, 679–686.

Masaldan, S., Clatworthy, S.A.S., Gamell, C., Meggyesy, P.M., Rigopoulos, A.-T., Haupt, S., Haupt, Y., Denoyer, D., Adlard, P.A., Bush, A.I., Cater, M.A., 2018. Iron accumulation in senescent cells is coupled with impaired ferritinophagy and inhibition of ferroptosis. Redox Biol. 14, 100–115.

Millner, A., Atilla-Gokcumen, G.E., 2020. Lipid players of cellular senescence. Metabolites 10, 339.

Moiseeva, O., Bourdeau, V., Roux, A., Deschênes-Simard, X., Ferbeyre, G., 2009. Mitochondrial dysfunction contributes to oncogene-induced senescence. Mol. Cell Biol. 29, 4495–4507.

Morales, J.C., Li, L., Fattah, F.J., Dong, Y., Bey, E.A., Patel, M., Gao, J., Boothman, D.A., 2016. Review of Poly (ADP-ribose) Polymerase (PARP) Mechanisms of Action and

Rationale for Targeting in Cancer and Other Diseases. Crit Rev Eukaryot Gene Expr 24 (1), 15–28.

Nakamura, T., Naguro, I., Ichijo, H., 2019. Iron homeostasis and iron-regulated ROS in cell death, senescence and human diseases. Biochim Biophys. Acta Gen. Subj. 1863, 1398–1409.

Olzmann, J.A., Carvalho, P., 2019. Dynamics and functions of lipid droplets. Nat. Rev. Mol. Cell Biol. 20, 137–155.

Onishi, M., Yamano, K., Sato, M., Matsuda, N., Okamoto, K., 2021. Molecular mechanisms and physiological functions of mitophagy. EMBO J. 40, e104705.

Park, J.T., Lee, Y.-S., Cho, K.A., Park, S.C., 2018. Adjustment of the lysosomal-mitochondrial axis for control of cellular senescence. Ageing Res. Rev. 47, 176–182.

Perry, D.K., Carton, J., Shah, A.K., Meredith, F., Uhlinger, D.J., Hannun, Y.A., 2000. Serine palmitoyltransferase regulates de novo ceramide generation during etoposide-induced apoptosis. J Biol Chem 275 (12), 9078–9084.

Picard, M., Shirihai, O.S., Gentil, B.J., Burelle, Y., 2013. Mitochondrial morphology transitions and functions: implications for retrograde signaling? Am J Physiol Regul Integr Comp Physiol. 304 (6), R393–406.

Pils, V., Terlecki-Zaniewicz, L., Schosserer, M., Grillari, J., Lämmermann, I., 2021. The role of lipid-based signalling in wound healing and senescence. Mech. Ageing Dev. 198, 111527.

Prasanna, P.G., Citrin, D.E., Hildesheim, J., Ahmed, M.M., Venkatachalam, S., Riscuta, G., Xi, D., Zheng, G., Deursen, J., van, Goronzy, J., Kron, S.J., Anscher, M.S., Sharpless, N.E., Campisi, J., Brown, S.L., Niedernhofer, L.J., O'Loghlen, A., Georgakilas, A.G., Paris, F., Gius, D., Gewirtz, D.A., Schmitt, C.A., Abazeed, M.E., Kirkland, J.L., Richmond, A., Romesser, P.B., Lowe, S.W., Gil, J., Mendonca, M.S., Burma, S., Zhou, D., Coleman, C.N., 2021. Therapy-induced senescence: opportunities to improve anticancer therapy. J. Natl. Cancer Inst. 113, 1285–1298.

Puig, S., Ramos-Alonso, L., Romero, A.M., Martínez-Pastor, M.T., 2017. The elemental role of iron in DNA synthesis and repair. Metallomics 9 (11), 1483–1500.

Stockwell, B.R., Friedmann Angeli, J.P., Bayir, H., Bush, A.I., Conrad, M., Dixon, S.J., Fulda, S., Gascón, S., Hatzios, S.K., Kagan, V.E., Noel, K., Jiang, X., Linkermann, A., Murphy, M.E., Overholtzer, M., Oyagi, A., Pagnussat, G.C., Park, J., Ran, Q., Rosenfeld, C.S., Salnikow, K., Tang, D., Torti, F.M., Torti, S.V., Toyokuni, S., Woerpel, K.A., Zhang, D.D., 2017. Ferroptosis: a regulated cell death nexus linking metabolism, redox biology, and disease. Cell 171, 273–285.

Suchanski, J., Grzegrzolka, J., Owczarek, T., Pasikowski, P., Piotrowska, A., Kocbach, B., Nowak, A., Dziegiel, P., Wojnar, A., Ugorski, M., 2018. Sulfatide decreases the resistance to stress-induced apoptosis and increases P-selectin-mediated adhesion: a two-edged sword in breast cancer progression. Breast Cancer Res. 20, 133.

Suckau, D., Resemann, A., Schuerenberg, M., Hufnagel, P., Franzen, J., Holle, A., 2003. A novel MALDI LIFT-TOF/TOF mass spectrometer for proteomics. Anal. Bioanal. Chem. 376, 952–965.

Tai, H., Wang, Z., Gong, H., Han, X., Zhou, J., Wang, X., Wei, X., Ding, Y., Huang, N., Qin, J., Zhang, J., Wang, S., Gao, F., Chrzanowska-Lightowlers, Z.M., Xiang, R.,

Xiao, H., 2017. Autophagy impairment with lysosomal and mitochondrial dysfunction is an important characteristic of oxidative stress-induced senescence. Autophagy 13, 99–113.

Takahashi, T., Suzuki, T., 2012. Role of sulfatide in normal and pathological cells and tissues. J. Lipid Res. 53, 1437–1450.

Thiele, H., Heldmann, S., Trede, D., Strehlow, J., Wirtz, S., Dreher, W., Berger, J., Oetjen, J., Kobarg, J.H., Fischer, B., Maass, P., 2014. 2D and 3D MALDI-imaging: conceptual strategies for visualization and data mining. Biochim. Biophys. Acta 117–137.

Torti, S.V., Torti, F.M., 2013. Iron and cancer: more ore to be mined. Nat. Rev. Cancer 13, 342–355.

Véquaud, E., Desplanques, G., Jézéquel, P., Juin, P., Barillé-Nion, S., 2016. Survivin contributes to DNA repair by homologous recombination in breast cancer cells. Breast Cancer Res Treat 155 (1), 53–63.

Wang, R., Qi, B., Dong, Y.W., Cai, Q.Q., Deng, N.H., Chen, Q., Li, C., Jin, Y.T., Wu, X.Z., 2016. Sulfatide interacts with and activates integrin αVβ3 in human hepatocellular carcinoma cells. Oncotarget 7, 36563–36576.

Wang, X., Tsao, S.-W., Wong, Y.-C., Cheung, A.L.M., 2003. Induction of senescent-like growth arrest as a new target in anticancer treatment. Curr. Cancer Drug Targets 3, 153–159.

Ward, R.J., Zucca, F.A., Duyn, J.H., Crichton, R.R., Zecca, L., 2014. The role of iron in brain ageing and neurodegenerative disorders. Lancet Neurol. 13, 1045–1060.

Wolrab, D., Jirásko, R., Cífková, E., Höring, M., Mei, D., Chocholoušková, M., Peterka, O., Idkowiak, J., Hrnčiarová, T., Kuchař, L., Ahrends, R., Brumarová, R., Friedecký, D., Vivo-Truyols, G., Škrha, P., Škrha, J., Kučera, R., Melichar, B., Liebisch, G., Burkhardt, R., Wenk, M.R., Cazenave-Gassiot, A., Karásek, P., Novotný, I., Greplová, K., Hrstka, R., Holčapek, M., 2022. Lipidomic profiling of human serum enables detection of pancreatic cancer. Nat. Commun. 13, 124.

Xie, Y., Hou, W., Song, X., Yu, Y., Huang, J., Sun, X., Kang, R., Tang, D., 2016. Ferroptosis: process and function. Cell Death Differ. 23, 369–379.

Yamasaki, T., Terai, S., Sakaida, I., 2011. Deferoxamine for advanced hepatocellular carcinoma. New Engl. J. Med. 365, 576–578.

Yambire, K.F., Rostosky, C., Watanabe, T., Pacheu-Grau, D., Torres-Odio, S., Sanchez-Guerrero, A., Senderovich, O., Meyron-Holtz, E.G., Milosevic, I., Frahm, J., West, A. P., Raimundo, N., 2019. Impaired lysosomal acidification triggers iron deficiency and inflammation in vivo. Elife 8, e51031.

Zellhofer, C.M., Beukelman, D.R., 1992. Service delivery in augmentative communication. Clin. Commun. Disord. 2, 7–18.

Zelnik, I.D., Ventura, A.E., Kim, J.L., Silva, L.C., Futerman, A.H., 2020. The role of ceramide in regulating endoplasmic reticulum function. Biochim Biophys Acta Mol Cell Biol Lipids 1865 (1), 158489.

Zhang, X., Chen, S., Huang, K., Le, W., 2013. Why should autophagic flux be assessed? Acta Pharm. Sin. 34, 595–599.